Scripta Materialia 256 (2025) 116429

Contents lists available at ScienceDirect

Scripta Materialia

journal homepage: www.journals.elsevier.com/scripta-materialia

Comparing molecular dynamics simulations of grain growth with experimental data

Meizhong Lyu [a], Zipeng Xu [b], Gregory S. Rohrer [b,1], Elizabeth A. Holm [a,*]

[a] Department of Materials Science and Engineering, University of Michigan, Ann Arbor, MI 48109, USA
[b] Department of Materials Science and Engineering, Carnegie Mellon University, Pittsburgh, PA 15213, USA

ARTICLE INFO

Keywords:
Molecular dynamics (MD)
Grain growth
Nickel
Grain boundaries

ABSTRACT

This study employed experimental data as the initial microstructure for molecular dynamics simulation of grain growth in polycrystalline nickel, aiming to investigate the relationship between grain boundary curvature and velocity in impurity-free systems. A bidirectional method for converting data between voxelized and atomic structures was developed and validated. The outcomes of the MD grain growth simulation broadly matched the characteristics of grain growth observed in the experiment. Most significantly, the simulation result contributes additional evidence supporting the reported absence of a correlation between velocity and curvature during grain growth in polycrystals, and confirms that this is not related to solutes, precipitates, processing route, or characterization method. The implication is that features of the 3D grain boundary network interfere with the velocity/curvature relationship.

Grain growth, which decreases system free energy by eliminating internal interfaces, is a fundamental microstructural evolution process in polycrystals. Despite more than 70 years of discussion, grain growth behavior remains incompletely understood. In the absence of other driving forces, the capillary driving force causes grain boundary motion. The capillary driving force is given by the weighted mean curvature $F = \gamma_{GB}\kappa$ where γ_{GB} is the grain boundary free energy per unit area and κ is the mean curvature [1,2]. Linear rate theory suggests that the grain boundary velocity v is proportional to the driving force, and that relationship is given by $v = M\gamma_{GB}\kappa$, where M is the mobility of the boundary; this relationship holds pointwise and when integrated over the boundary as a whole [3–5]. The correlation between velocity and mean curvature has been verified through experimental studies [4,6,7] and simulations [8] of grain boundary migration in bicrystals. However, some recent experiments report the surprising observation that there is no apparent correlation between mean curvature and velocity during grain growth in polycrystalline nickel [9], $SrTiO_3$ [10], and α-Fe [11].

Much research on three-dimensional grain growth theory relies on computational simulation. On one hand, achieving non-destructive and high-resolution characterization in experiments is still a challenge [12]. On the other hand, measurements must be conducted in truly pure materials to minimize the impact of impurities on grain boundary migration [13,14]. In contrast, computational simulation allows for modeling grain boundary motion in pure materials and extracting the microstructure features easily. Most grain growth theories are explored through continuum simulations, including isotropic [15,16] and anisotropic [17–19] grain growth. To assess the capability of simulations in capturing pathways and grain boundary properties during grain growth, some studies report comparisons with experimental observations [20–22]. The results indicate a statistical consistency in the grain growth kinetics, but the simulations typically do not capture individual grain evolution trajectories, including topological changes. This is attributed to neglecting the anisotropic crystalline nature of grain boundaries in the continuum simulation.

In contrast, molecular dynamics (MD) simulation does not rely on assumptions about the grain boundary migration mechanism during grain growth. The anisotropy of grain boundary energy and mobility is inherently present in the atomic configurations [23]. Additionally, MD simulation can eliminate interference from impurities that might exist in experimental samples and only model evolution in pure materials. Due to computational limitations, current MD simulations of grain growth must be carried out at the nanoscale. There have been no reported

* Corresponding author.
E-mail address: eaholm@umich.edu (E.A. Holm).
[1] Greg Rohrer was an Editor of the journal during the review period of the article. To avoid a conflict of interest, Greg Rohrer was blinded to the record and another editor processed this manuscript.

https://doi.org/10.1016/j.scriptamat.2024.116429
Received 22 April 2024; Received in revised form 20 September 2024; Accepted 17 October 2024

comparisons between atomistic simulations of grain growth and experimental results in three dimensions. This is partly due to the difficulty in acquiring large-scale and high-fidelity experimental data suitable for comparison with grain growth simulations. In addition, there is a need to develop a method for transforming the experimental data into the initial microstructure for MD simulation; most MD grain growth simulations begin with a Voronoi tessellation [24–26].

The existing methods of constructing computational microstructures from experimental data typically involve defining a surface mesh [27, 28]. After obtaining the enclosing surface, atoms are filled into volume to create a crystal that satisfies the crystallographic information, using codes such as nanoSCULPT [28]. However, the construction of a surface mesh from data points introduces a certain level of error, which may have a significant impact on the precision of the constructed atomic-scale microstructure. As an alternate approach, we present our methodology that transforms the experimental voxel-based structure directly into the atomic-based structure for simulation.

We assume that the atomistic polycrystalline FCC structure can be seen as an assembly of multiple individual FCC grains, and each grain can be obtained by "sculpting" a sphere. The experimental data are represented in voxel-based form (Fig. 1a), and the Cartesian coordinates of the initial experimental data serve as the reference frame. For each voxel-based grain from the experiment ($Grain_{VB\text{-}ref}$), we initially determine the bounding box diagonal and generate a three-dimensional sphere with this length as the diameter. Then a grid of points with the same orientation as the reference frame is generated over the interior of the three-dimensional sphere, referred to as the Base Ball ($Ball_{VB}$, depicted in Fig. 1b). The voxel edge length in $Ball_{VB}$ (L_{BALL}) has a scaling relationship with the size of the voxel in the experimental data (L_{EXP}), and the ratio (L_{EXP}/ L_{BALL}) is defined as the cube ratio (Fig. 1b).

The FCC lattice ($Ball_{FCC}$) can be easily obtained by adding points within $Ball_{VB}$, with the number of points in $Ball_{FCC}$ being four times that in $Ball_{VB}$ (Fig. 1c). Then the $Ball_{FCC}$ is rotated with its center based on the crystallographic orientation of $Grain_{VB\text{-}ref}$ ($Ball_{FCC\text{-}oriented}$, depicted in Fig. 1d), ensuring that $Ball_{FCC}$ has the same grain orientation relative to the reference frame. Finally, the $Grain_{VB\text{-}ref}$ is placed at the center of the $Ball_{FCC\text{-}oriented}$ for "sculpting" (Fig. 1e). The neighborhood search algorithm is employed to obtain all atoms within $\sqrt{2}L_{BALL}$ from each voxel in $Grain_{VB\text{-}ref}$, and these atoms constitute the rough FCC grains ($Grain_{FCC\text{-}rough}$, depicted in Fig. 1f). Intuitively, a smaller cube ratio, with 1 considered as the smallest effective cube ratio, would result in a larger "sculpted" $Grain_{FCC\text{-}rough}$.

To ensure a close match with the grain boundaries in voxel-based experimental data, it is necessary to refine the structure of the transition region between two neighboring grains. Therefore, the $Grain_{VB\text{-}ref}$ in the former "sculpting" step should encompass not only the voxel grid specific to that grain ($Grain_{VB\text{-}self}$) but also the grids from all neighboring grains within L_{EXP} ($Grain_{VB\text{-}NN}$) to preserve the voxel-based grain boundary throughout the "sculpting" step. Some atoms in $Grain_{FCC\text{-}rough}$ might extend beyond the range of $Grain_{VB\text{-}self}$. If the nearest grid point of an atom belongs to $Grain_{VB\text{-}self}$, then this atom is kept as a part of the grain boundary. Otherwise, it is deleted. The atoms in the final atomic-based grain will all be contained within the $Grain_{VB\text{-}self}$, as shown in Fig. 1g.

The high-purity polycrystalline nickel structure used in the experiment originated from a 1 mm diameter nickel wire and was stored in a voxel-based structure comprised of voxels that are 2.8 μm × 2.8 μm × 4 μm [9]. The acquisition of these data by high energy diffraction microscopy has been described previously [9,29] and the data are publicly available [30]. A summary of the data acquisition is provided in the supplemental materials. To obtain the largest initial microstructure for MD simulation, we cropped the largest inscribed rectangular cuboid within the disk-shaped experimental data volume (with dimensions of 220 × 220 × 60 voxels), as shown in Fig. 2a. No special treatment was applied to the boundary of the initial microstructure; to accommodate the simulation boundary conditions, we allowed edge grains to contact each other via periodic boundary conditions. This approach simplified the MD simulations while ensuring a local environment for the grains at

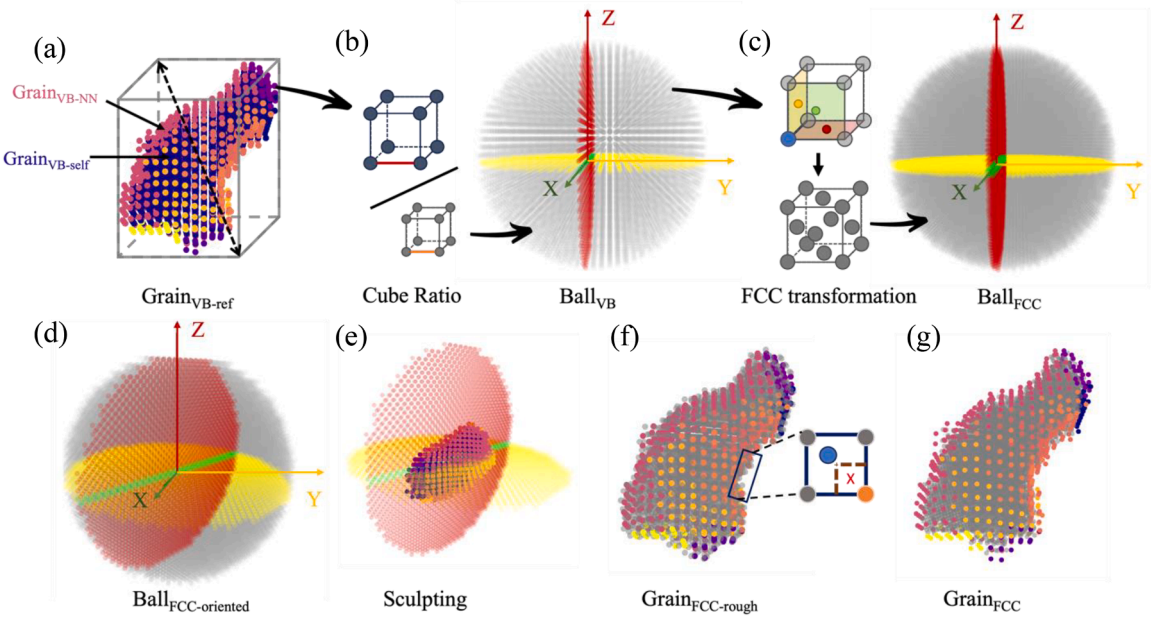

Fig. 1. The procedure for transforming a voxelated grain into an oriented atomic structure. (a) Select voxel-based grain from experimental data as $Grain_{VB\text{-}ref}$, which consists of $Grain_{VB\text{-}self}$ (the voxels possess the same ID with the selected grain, dark colored) and $Grain_{VB\text{-}NN}$ (the voxels from the nearest neighbor grains, light colored) The bounding box diagonal of $Grain_{VB\text{-}ref}$ is extracted as the diameter for the Base Ball. (b) Choose an appropriate cube ratio to build voxel-based Base Ball ($Ball_{VB}$). Cube ratio is defined as the ratio of the voxel's length between $Grain_{VB\text{-}ref}$ and $Ball_{VB}$. The Cartesian coordinate is the same as the experimental data and serves as reference frame. (c) Expand $Ball_{VB}$ to FCC-based Base Ball ($Ball_{FCC}$). The FCC lattice is formed by adding three points to the face center according to each point in the voxel grid. (d) Rotate the $Ball_{FCC}$ based on the grain orientation ($Ball_{FCC\text{-}oriented}$). (e) Place the $Grain_{VB\text{-}ref}$ at the center of $Ball_{FCC\text{-}oriented}$ for sculpting. (f) The comparison between atomic-based grain after sculpting ($Grain_{FCC\text{-}rough}$, gray colored) and $Grain_{VB\text{-}NN}$ (light colored). Apply distance-based criteria to filter grain boundary atoms within $Grain_{FCC\text{-}rough}$. (g) The final atomic-based grain ($Grain_{FCC}$), which all atoms are within the $Grain_{VB\text{-}NN}$.

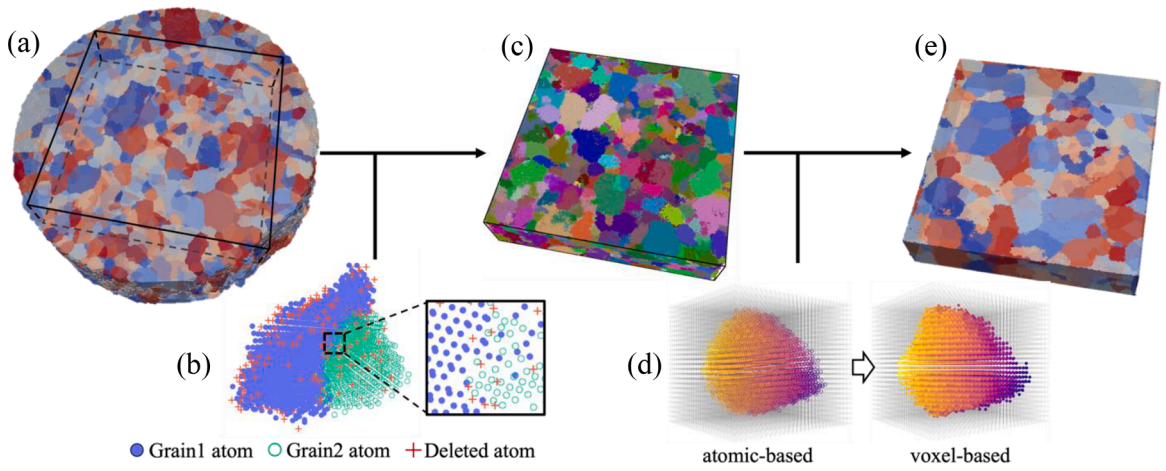

Fig. 2. Microstructure processing. (a) The voxel-based experimental microstructure, where colors are used to distinguish between different grains. The volume for voxel-atomic conversion is defined by the largest inscribed rectangular cuboid as shown. (b) Illustration of atom deletion within the cutoff distance during the assembly of individual grains. (c) Initial atomic-based microstructure for MD simulation, and colors are employed to differentiate between grain IDs. (d) Schematic depiction of the reconstruction of a voxel-based structure (right) by using a 3D grid (grey points) to scan the nearest atoms in atomic-based structure (left). (e) The reconstructed voxel-based final simulation structure in Dream3D. Colors are used to distinguish between different grains.

the center of the microstructure similar to that in the experiment. All voxel-based grains within this volume were independently transformed into atomic-based grains as described above. The polycrystalline structure was then scaled to units of Angstroms, using the ratio of the lattice constant divided by the cube ratio. The Open Visualization Tool (OVITO) [31] modifiers were applied to filter and remove atoms within a cutoff distance of 1.6 Å in the region between the neighboring grains, which is illustrated in Fig. 2b. We chose the cube ratio as 1.5 in this study as a trade-off between the resolution of the atomic structure and the required computing resources. The size ratio of the voxel-based grain to the atomic-based grain was approximately 0.9, where the initial microstructure, in Fig. 2c, contains 4688,370 atoms and dimensions of 610.40 $\mathring{A}$ × 610.40 $\mathring{A}$ × 141.76 Å. This microstructure encompassed a total of 1911 grains.

All grain growth simulations were performed using LAMMPS [32] with the Foiles-Hoyt Embedded Atom Method (EAM) potential for nickel [33]. A time step of 0.002 ps (2 fs) was used for all dynamics simulations, and periodic boundary conditions were employed in all three Cartesian directions. Energy minimization was first applied to relax the transformed atomic-based structure completely. The microstructure was heated from 50 K to 650 K over 1.2 ns and annealed at 650 K for another 0.4 ns, using an isothermal-isobaric NPT ensemble. A dump file was saved at intervals of 0.05 ns. The simulation parameters were chosen based on the alignment method described below.

To compare the microstructural evolution in the grain growth simulation with experiments, it is necessary to establish a standard for aligning the experimental and simulation data. (In essence, we match simulation and experimental annealing times, recognizing that the actual time scales are vastly different.) Here, we applied the same post-processing methods to all experimental and simulation structures (described below), including cropping, voxel-atomic conversion, and grain segmentation with the OVITO modifiers. We selected the five simulation outputs with the closest average grain size to the corresponding experimental structures. Then, the grain tracking algorithm was used to unify the grain IDs in all selected simulation outputs. The microstructure in the last simulation output comprises 280 grains tracked from the initial structure.

To maintain consistency with experimental methods in the subsequent calculations of grain boundary curvature and velocities, we need to convert the atomic-based structure back to the voxel-based structure using a method similar to voxel-atomic conversion. We generated a 3D voxel grid with a dimension of 608 $\mathring{A}$ × 608 $\mathring{A}$ × 142 Å, which was constructed with voxels that are 2 $\mathring{A}$ × 2 $\mathring{A}$ × 2 Å. For each voxel, the distance algorithm was used to find the nearest atom in the simulation structures and assign the atomic orientation to the voxel. The atomic-voxel conversion is illustrated in Fig. 2d. Then, we imported the voxel-based simulation structures into Dream3D [34] to reconstruct the microstructure (Fig. 2e). After surface meshing and smoothing [35], the resulting grain boundaries are represented using triangular elements. All five macroscopic grain boundary parameters can be obtained from the triangles. The overall grain boundary velocity is quantified based on the number of exchanged voxels near the grain boundary, using the method described in [9]. The integral mean curvature is obtained by averaging the curvature of all mesh triangles in the grain boundary [11]. Because the velocity and curvature calculations depend on the details of the mesh elements, the segmentation and smoothing parameters represent a source of uncertainty. In addition, we note that we cannot include the energetic contribution to the weighted mean curvature, since we do not know the surface free energy at every point along the boundary.

The grain boundary population as a function of the disorientation angle is given in Fig. 3a. Except for the local maxima at 39° (Σ9) and 60° (Σ3), the data follows Mackenzie's distribution for randomly oriented cubes [36]. The values of the distribution below 2° are negligible due to the misorientation threshold set between the neighboring grains. These crystallographic features agree with the experimental structure, validating the conversion methodology [37,38].

The relationship between the average grain boundary velocity and curvature is given in Fig. 3b. The curvatures are binned in intervals of 0.0015 $Å^{-1}$, and the red markers in the plot represent the means of the velocity in each bin; error bars indicate the standard deviation. To minimize the influence of noise on the results, we chose a curvature of 0.03 $Å^{-1}$ as the cutoff condition, with over 90 % of the grain boundary curvature falling below this threshold. The grain boundaries with higher curvature were excluded due to insufficient observations, which could introduce noise and inaccurately represent the relationship between the average velocity and curvature.

In Fig. 3b, it can be observed that there is a slight positive correlation between average velocity and curvature when the curvature is very small (less than 0.0045 $Å^{-1}$). However, no obvious correlation between velocity and curvature is observed when curvature exceeds 0.009 $Å^{-1}$. The large error bars corresponding to each curvature bin in Fig. 3b indicate that GBs with similar mean curvatures have very different velocities. This can be explained by the fact that grain boundary migration depends on the surrounding microstructural environment and is

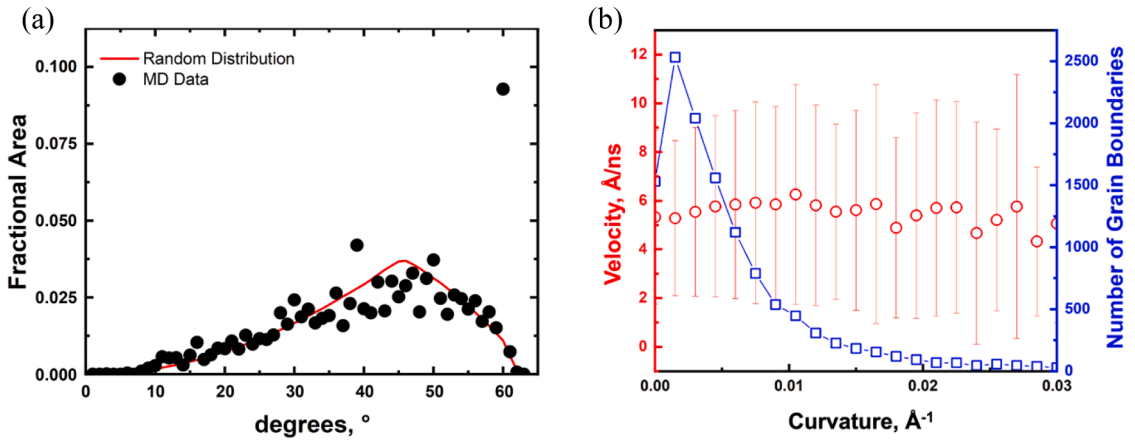

Fig. 3. (a) Disorientation angle distribution for 12,582 grain boundaries in combined voxel-based simulation structures. (b) Mean grain boundary velocity as a function of mean curvature for 90 % of the grain boundaries (red). The curvature values are grouped into bins of width 0.0015 $Å^{-1}$, and the distribution of boundary curvatures is shown in blue.

influenced by factors beyond the mean curvature. Factors that can alter the motion of high-curvature grain boundaries include impurities, crystallographic anisotropy in grain boundary mobility or energy, the drag effect induced by triple junctions [39] and disconnection modes [40], and stresses that arise from shear coupled boundary motion [41, 42].

The relationship between average velocity and mean curvature calculated in the MD simulations is similar to the result reported in the experimental work with the same Ni sample by Bhattacharya et al. [9]. The agreement between simulation and experiment, despite significant differences in length and time scales, implies that *the lack of correlation between boundary mean curvature and velocity is a fundamental feature of grain growth in polycrystals*. It cannot be attributed to solute or precipitate pinning, nor to processing-related or characterization artifacts. It is well-established that grain boundaries in MD bicrystals do migrate by mean curvature [8]. This implies that features inherent in the 3D grain boundary network are responsible for erasing the velocity/curvature correlation. For example, triple lines may directly inhibit grain growth [39], or they may interact with grain boundary disconnections to interfere with boundary motion [40]. In addition, even in the absence of triple lines, dimensional constraints will inhibit the shear displacement required for normal motion of shear coupled grain boundaries [41,42]. Note that within the scope of this study, we cannot draw conclusions about the contributions of these motion inhibition mechanisms. Clearly, there is a need for further theoretical and experimental analysis to understand the breakdown of the curvature/velocity relationship.

Fig. 4a illustrates the variations in grain boundary velocity for Σ3= 60°/[111] misorientation, and Fig. 4b and c show the grain boundary curvature and relative area respectively. There were no systematic differences in the calculation of velocity distribution for each timestep, so

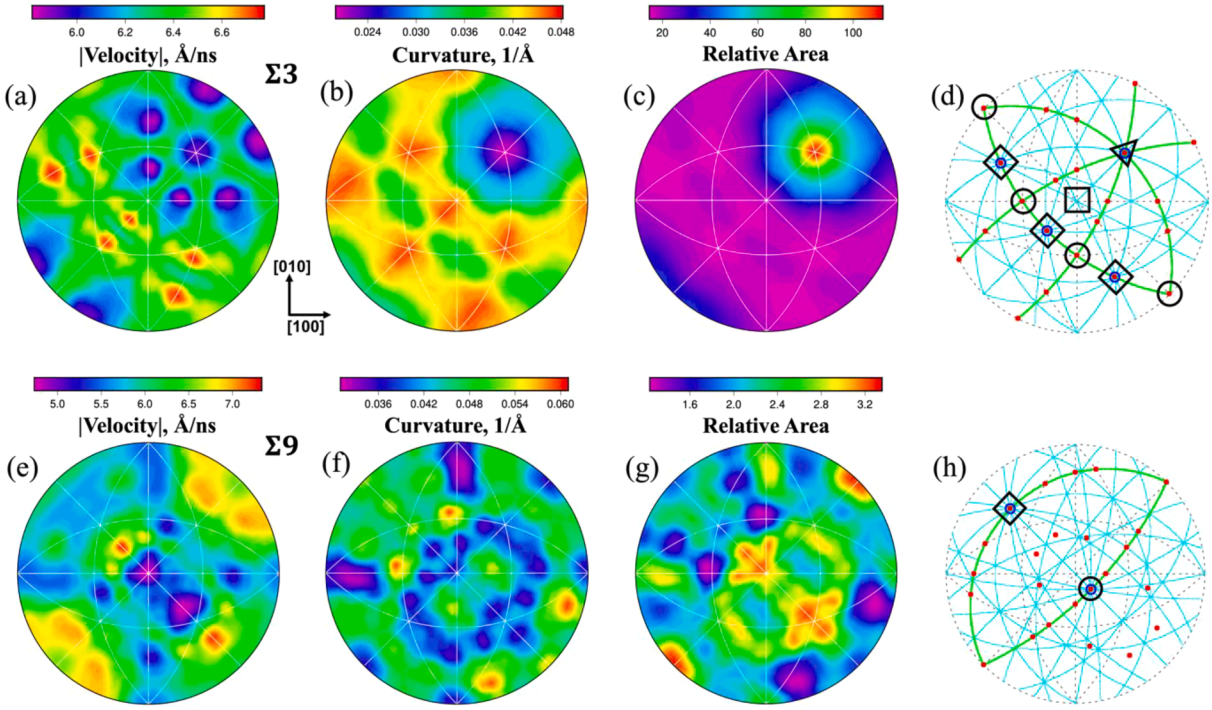

Fig. 4. Grain boundary velocity, curvature, and relative area distribution for Σ3 (a–c) and Σ9 (e–g) grain boundaries plotted in stereographic projections along [001]. Two stereographic projections (d and f) were generated in GBTool box [43]. (d) The orientations marked with circles, diamonds and triangle are $\{\bar{2}11\}$ STGBs, $\{\bar{1}01\}$ tilt boundaries and the {111} twist boundaries, respectively. (h) The orientation marked with circle and diamond are {114} STGBs and {221} STGBs, respectively.

the data from all of the time steps are combined and considered together. These distributions are calculated from 981,919 triangles from 208 different boundaries. The relative grain boundary area exhibits an inverse correlation with curvature; that is, flat boundaries tend to be larger. The minimum velocity corresponds to the coherent twin boundaries at (111) orientation, which are also the lowest curvature boundaries. The tilt boundaries at the $\{\bar{2}11\}$ orientation have the maximum velocities and also higher curvatures.

The $\Sigma 9 = 39.9°/[110]$ misorientation also shows a relatively high population in the disorientation distribution (Fig. 3a). Fig. 4(e–g) show the grain boundary velocity, curvature, and relative area for these boundaries. These distributions are calculated from 248,631 triangles from 120 different grain boundaries. Like the Σ3 boundaries, the grain boundary relative area is inversely proportional to the curvature distribution, but there is no strong correlation observed between the velocity distribution and curvature. These results broadly agree with the corresponding experimental observations [9].

Recall that the simulation data suggest a slight positive correlation between velocity and curvature only for boundaries with very low curvatures; this is not seen in the experimental results. A similar observation is made in MD simulations of nanocrystalline grain growth in Al, which show a correlation between velocity and curvature for Σ3 coherent twin boundaries but no others [24]. This might be attributed to the difference in defect density and spatial length between the experiment (microscale) and MD simulation (nanoscale). In FCC metals, boundaries with very low curvature (i.e. flat boundaries) are often faceted coherent Σ3 twin boundaries, as shown in Fig. 4b and c. The density of the defects that permit boundary motion (e.g. dislocations and disconnections) can be quite low in faceted boundaries. While a micron-scale boundary may contain enough defects for motion, a nanoscale boundary may contain none at all [44], significantly inhibiting its motion. Therefore, compared to real materials, the flat boundaries in simulations are more likely to be of low velocity. On the other hand, even at the nanoscale, more highly curved and nonfaceted grain boundaries like the Σ9 boundaries in Fig. 4f are likely to have significant defect content, increasing the potential for grain boundary motion. Thus, there is no obvious correlation between grain boundary velocities and curvatures for high-curvature grain boundaries, an observation that aligns with the findings in experiments. If this explanation is correct, it implies that a grain boundary's mobility is extrinsic and depends on its size and defect content [45–48], causing the grain boundary motion to be not only a normal displacement of the interface.

In conclusion, we developed a voxel-atomic bidirectional conversion method and converted a 3D experimental microstructure into the initial structure for an MD simulation of grain growth. When comparing the outcomes of the MD grain growth simulation with the experimental data, the distinct characteristics of grain growth in nickel polycrystals were observed, and the correlation between grain boundary velocity and curvature matched the surprising conclusions drawn from the experiments. Our atomistic simulation result contributes additional evidence supporting the widespread absence of a correlation between velocity and curvature during grain growth in polycrystals, and we confirm that this is not related to solutes, precipitates, processing routes, or characterization methods. The implication is that features of the 3D grain boundary network, which include topological constraints, defect interactions, and shear coupling effects, interfere with the velocity/curvature relationship.

CRediT authorship contribution statement

Meizhong Lyu: Writing – original draft, Visualization, Validation, Software, Resources, Methodology, Investigation, Formal analysis, Data curation, Conceptualization. **Zipeng Xu:** Writing – review & editing, Validation, Methodology, Formal analysis, Data curation. **Gregory S. Rohrer:** Writing – review & editing, Supervision, Methodology, Funding acquisition, Data curation. **Elizabeth A. Holm:** Writing – review & editing, Supervision, Resources, Project administration, Methodology, Funding acquisition, Conceptualization.

Declaration of competing interest

The authors declare the following financial interests/personal relationships which may be considered as potential competing interests:

Elizabeth A. Holm reports financial support was provided by University of Michigan. If there are other authors, they declare that they have no known competing financial interests or personal relationships that could have appeared to influence the work reported in this paper.

Acknowledgments

This work was supported by the National Science Foundation under DMREF grant DMR-2118945. This work used Bridges-2 at Pittsburgh Supercomputing Center through allocation MAT220017P from the Advanced Cyberinfrastructure Coordination Ecosystem: Services & Support (ACCESS) program, which is supported by National Science Foundation grants #2138259, #2138286, #2138307, #2137603, and #2138296.

Supplementary materials

Supplementary material associated with this article can be found, in the online version, at doi:10.1016/j.scriptamat.2024.116429.

References

[1] J.E. Burke, D. Turnbull, Recrystallization and grain growth, Prog. Met. Phys. 3 (1952) 220–292.
[2] J.E. Taylor, II—Mean curvature and weighted mean curvature, Acta Metall. Mater. 40 (7) (1992) 1475–1485.
[3] Beck P.A.. Interface migration in recrystallization. Metal interfaces. American Society for Testing Materials, Cleveland, 1952. pp. 208–247.
[4] R.A. Vandermeer, D.J. Jensen, E. Woldt, Grain boundary mobility during recrystallization of copper, Metall. Mater. Trans. A 28 (1997) 749–754.
[5] JE. Taylor, JW. Cahn, CA. Handwerker, Overview No. 98 I—Geometric models of crystal growth, Acta Metall. Mater. 40 (7) (1992) 1443–1474.
[6] C. Günster, D.A. Molodov, G. Gottstein, Migration of grain boundaries in Zn, Acta Mater. 61 (7) (2013) 2363–2375.
[7] D.A. Molodov, L.A. Barrales-Mora, J.E Brandenburg, Grain boundary motion and grain rotation in aluminum bicrystals: recent experiments and simulations, IOP Conf. Ser. Mater. Sci. Eng. 89 (1) (2015) 012008. IOP Publishing.
[8] M. Upmanyu, R.W. Smith, D.J. Srolovitz, Atomistic simulation of curvature driven grain boundary migration, Interface Sci. 6 (1998) 41–58.
[9] A. Bhattacharya, Y.F. Shen, C.M. Hefferan, et al., Grain boundary velocity and curvature are not correlated in Ni polycrystals, Science 374 (6564) (2021) 189–193 (1979).
[10] V. Muralikrishnan, et al., Observations of unexpected grain boundary migration in $SrTiO_3$, Scr. Mater. 222 (2023) 115055.
[11] Z. Xu, et al., Grain boundary migration in polycrystalline α-Fe, Acta Mater. 264 (2024) 119541.
[12] A.J. Shahani, X. Xiao, E.M. Lauridsen, et al., Characterization of metals in four dimensions, Mater. Res. Lett. 8 (12) (2020) 462–476.
[13] L.S. Shivindlerman, G. Gottstein, D.A Molodov, Grain boundary motion in pure metals: effect of interaction between adsorbed atoms at moving boundaries, Phys. Status Solidi A 160 (2) (1997) 419–429.
[14] H. Zhang, M.I. Mendelev, D.J. Srolovitz, Computer simulation of the elastically driven migration of a flat grain boundary, Acta Mater. 52 (9) (2004) 2569–2576.
[15] C.E. Krill III, L.Q. Chen, Computer simulation of 3-D grain growth using a phase-field model, Acta Mater. 50 (12) (2002) 3059–3075.
[16] E. Miyoshi, T. Takaki, M. Ohno, et al., Ultra-large-scale phase-field simulation study of ideal grain growth, npj Comput. Mater. 3 (1) (2017) 25.
[17] H. Hallberg, V.V Bulatov, Modeling of grain growth under fully anisotropic grain boundary energy, Model. Simul. Mater. Sci. Eng. 27 (4) (2019) 045002.
[18] M. Elsey, S. Esedog, P. Smereka, Simulations of anisotropic grain growth: efficient algorithms and misorientation distributions, Acta Mater. 61 (6) (2013) 2033–2043.
[19] J.D. Niño, O.K. Johnson, Influence of grain boundary energy anisotropy on the evolution of grain boundary network structure during 3D anisotropic grain growth, Comput. Mater. Sci. 217 (2023) 111879.
[20] J. Zhang, W. Ludwig, Y. Zhang, et al., Grain boundary mobilities in polycrystals, Acta Mater. 191 (2020) 211–220.
[21] I.M. McKenna, S.O. Poulsen, E.M. Lauridsen, et al., Grain growth in four dimensions: a comparison between simulation and experiment, Acta Mater. 78 (2014) 125–134.

[22] X. Peng, A. Bhattacharya, S.K. Naghibzadeh, et al., Comparison of simulated and measured grain volume changes during grain growth, Phys. Rev. Mater. 6 (3) (2022) 033402.
[23] S. Okita, E. Miyoshi, S. Sakane, et al., Grain growth kinetics in submicrometer-scale molecular dynamics simulation, Acta Mater. 153 (2018) 108–116.
[24] G.B. Bizana, L.A. Barrales-Mora, 3D grain growth in nanocrystalline Al via molecular dynamics: influence of size, topology and integral mean curvature on grain kinetics, Comput. Mater. Sci. 219 (2023) 112009.
[25] Y. Hu, J. Xu, L. Su, et al., Tensile responses of polycrystalline Mo via molecular dynamics simulation: grain size and temperature effects, Mater. Chem. Phys. 296 (2023) 127270.
[26] V.V. Dremov, P.V. Chirkov, A.V. Karavaev, Molecular dynamics study of the effect of extended ingrain defects on grain growth kinetics in nanocrystalline copper, Sci. Rep. 11 (1) (2021) 934.
[27] C. Lv, W. Lin, B. Zhao, Voxel structure-based mesh reconstruction from a 3D point cloud, IEEE Trans. Multimed. 24 (2021) 1815–1829.
[28] A. Prakash, M. Hummel, S. Schmauder, et al., Nanosculpt: a methodology for generating complex realistic configurations for atomistic simulations, MethodsX 3 (2016) 219–230.
[29] M. Hefferan, S.F. Li, J. Lind, U. Lienert, A.D. Rollett, P. Wynblatt, R.M. Suter, Statistics of high purity nickel microstructure from high energy X-ray diffraction microscopy, CMC Comput. Mater. Contin. 14 (2009) 209–219.
[30] G.S. Rohrer, (2024) http://mimp.materials.cmu.edu/~gr20/Grain_Boundary_Data_Archive/Ni_velocity/Ni_velocity.html.
[31] A. Stukowski, Visualization and analysis of atomistic simulation data with OVITO–the open visualization tool, Model. Simul. Mater. Sci. Eng. 18 (1) (2009) 015012.
[32] A.P. Thompson, et al., LAMMPS-a flexible simulation tool for particle-based materials modeling at the atomic, meso, and continuum scales, Comput. Phys. Commun. 271 (2022) 108171.
[33] S.M. Foiles, J.J. Hoyt, Computation of grain boundary stiffness and mobility from boundary fluctuations, Acta Mater. 54 (12) (2006) 3351–3357.
[34] M.A. Groeber, M.A. Jackson, DREAM.3D: a digital representation environment for the analysis of microstructure in 3D, Integr. Mater. Manuf. Innov. 3 (2014) 5.
[35] D.A. Field, Laplacian smoothing and Delaunay triangulations, Commun. Appl. Numer. Methods 4 (6) (1988) 709–712.
[36] J.K. Mackenzie, M.J. Thomson, Some statistics associated with the random disorientation of cubes, Biometrika 44 (1–2) (1957) 205–210.
[37] V. Randle, et al., Five-parameter grain boundary distribution of commercially grain boundary engineered nickel and copper, Acta Mater. 56 (10) (2008) 2363–2373.
[38] J. Li, SJ. Dillon, GS. Rohrer, Relative grain boundary area and energy distributions in nickel, Acta Mater. 57 (14) (2009) 4304–4311.
[39] G. Gottstein, L.S. Shvindlerman, B. Zhao, Thermodynamics and kinetics of grain boundary triple junctions in metals: recent developments, Scr. Mater. 62 (12) (2010) 914–917.
[40] C. Wei, et al., A continuum multi-disconnection-mode model for grain boundary migration, J. Mech. Phys. Solids 133 (2019) 103731.
[41] F. Ulomek, V. Mohles, Separating grain boundary migration mechanisms in molecular dynamics simulations, Acta Mater. 103 (2016) 424–432.
[42] J.W. Cahn, J.E. Taylor, A unified approach to motion of grain boundaries, relative tangential translation along grain boundaries, and grain rotation, Acta Mater. 52 (16) (2004) 4887–4898.
[43] K. Glowinski, A. Morawiec, A toolbox for geometric grain boundary characterization, in: Proceedings of the 1st International Conference on 3D Materials Science, Springer International Publishing, 2016.
[44] D.G. Morris, The origins of strengthening in nanostructured metals and alloys, Revista de Metalurgia 46 (2) (2010) 173–186.
[45] C.P. Race, et al., Mechanisms and kinetics of the migration of grain boundaries containing extended defects, Phys. Rev. B 92 (17) (2015) 174115.
[46] A. Qiu, I. Chesser, E. Holm, On the variability of grain boundary mobility in the isoconfigurational ensemble, Acta Mater. 257 (2023) 119075.
[47] S.L. Thomas, et al., Reconciling grain growth and shear-coupled grain boundary migration, Nat. Commun. 8 (1) (2017) 1764.
[48] J. Han, SL. Thomas, D.J. Srolovitz, Grain-boundary kinetics: a unified approach, Prog. Mater. Sci. 98 (2018) 386–476.